Facile synthesis of highly efficient Pt/N-rGO/N-NaNbO₃ nanorods toward photocatalytic hydrogen production

Fengli Yang, Quan Zhang, Lu Zhang, Mengting Cao, Qianqian Liu, Wei-Lin Dai*

Department of Chemistry and Shanghai Key Laboratory of Molecular Catalysis and Innovative Materials, Fudan University, Shanghai 200433, PR China

ABSTRACT

Highly efficient and stable Pt/N-rGO/N-NaNbO₃ nanorod photocatalysts were prepared by a facile two-step hydrothermal method for the first time. An excellent hydrogen evolution rate of $2342\,\mu mol\,g^{-1}\,h^{-1}$ is attained by 0.5%Pt/0.5%N-rGO/N-NaNbO₃ under mimic sunlight irradiation, which is evidently higher than those of both the pristine NaNbO₃ nanorod ($241\,\mu mol\,g^{-1}\,h^{-1}$) presented in this work and several modified NaNbO₃ catalysts reported in the preceding literatures. Such a huge improvement in the photocatalytic performance is mainly attributed to the narrowed band gap of NaNbO₃ nanorod by the doping of nitrogen element, the increased light absorption over the entire range of wavelength by the introduction of N-rGO, and the reduced electron-hole recombination rate by the excellent electron transfer properties of N-rGO and Pt nanoparticles. This innovative work may suggest a meaningful approach for developing a more appealing and practical method to modify sodium niobate for photocatalytic hydrogen generation.

1. Introduction

Nowadays, the environmental pollution and the scarcity of fossil fuels have become two conflicting concerns that threaten the development and even survival of human beings. With the substantial growth of economy and the improvement of environmental awareness, people worldwide are striving to search for alternative energy sources. The research on hydrogen production, as one of them, has therefore been popularizing, while photocatalytic water-splitting hydrogen evolution is a promising technology to generate it. Accordingly, looking for new and highly efficient photocatalysts has been a research hotspot. So far, there have been a large number of semiconductor materials for photocatalytic hydrogen production, such as TiO₂ [1], g-C₃N₄ [2,3], CdS [4], SrTiO₃ [5]. Among these, environmentally perovskites have garnered quite noticeable attention, for its outstanding dielectric properties and perovskite structure [6–8].

Among perovskites, sodium niobate (NaNbO₃) has attracted considerable attention in both scientific and engineering fields for good chemical stability, low cost, high abundance, and environmental friendliness [9,10]. Recent researches show that NaNbO₃ is able to play a noticeable role in H₂ generation, CO₂ reduction and degradation of pollutants due to its unique structures and properties [11–14]. Nevertheless, its inherent rapid recombination rate of photoexcited electron-hole pairs and wide band gap both restrict its photocatalytic activity. To

address this issue, various strategies have been devoted to narrow its band gap and speed up the separation of electron-hole pairs, improving its photocatalytic activity including coupling with low bandgap semiconductors, self-doping or doping with other elements [15,16]. Coupling NaNbO₃ with other materials (e.g., CdS [17], BiOI [18], CaZrO₃ [19]) to develop composite photocatalysts is presented to be an efficient approach for improving its photocatalytic activity.

Metal particles (such as Au, Ag and Pt) loaded semiconductors have exhibited a shining prospective for improving the photocatalytic activity of niobates. On the one hand, due to the energy band alignment, the loading of metal particles on the semiconductor improves the charge separation efficiency. On the other hand, owing to the lower Fermi energy level of the metal conduction potential, the conduction electrons of the semiconductor can be injected into noble metals through the metal/semiconductor interface, and these electrons will effectively participate in the catalysis [20,21]. Among metal loaded semiconductor system, Pt-based composite is currently recognized as one of the most effective catalysts for H₂ evolution, primarily because Pt particles can improve electron-hole separation through acting as electron traps, and decrease overpotential for water splitting as well.

Another interesting approach to decrease the photoinduced electron-hole pair recombination rate is to refine the electron transfer by utilizing conductive carbon materials. In recent years, reduced graphene oxide (rGO) has attracted considerable attention for its various

potential applications thanks to its superior charge carrier mobility properties, ultrathin thickness, large specific surface, structural flexibility and physicochemical stability [22,23]. Due to its excellent electron mobility and low-resistance pathways, efficient separation of photoexcited electron-hole pairs at interface can be easily achieved, causing the boost of the photocatalytic activity [24,25]. However, rGO does not display high electronic conductivity because of its incomplete sp2-hybridized network. So far, theoretical and experimental studies have shown that the electronic properties of rGO can be rationally tuned through various chemical methods. Heteroatom doping, one of the most significant methods, is well-known to modify the possibly optimized electronic structure and properties of graphene [26–28]. In particular, N-doping can effectively modulate the chemical reactivity and electron-donor properties of graphene, for the reason that nitrogen has stronger electron negativity than carbon and the nitrogen lone electron pairs are conjugated to the graphene π-system. With such particular properties, nitrogen-doped rGO is currently applied in many fields including lithium ion battery [29] and catalytic reactions [30,31].

Herein, in this study, $NaNbO_3$ and rGO are employed as two candidates for constructing N-rGO/N-$NaNbO_3$ composite photocatalysts, and then Pt NPs are evenly distributed on the surface of N-rGO/N-$NaNbO_3$. This work introduces the preparation and characterization of novel Pt/N-rGO/N-$NaNbO_3$ composite through a facile two-step method for the first time, and the nanocomposites are characterized utilizing X-ray diffraction (XRD), Raman spectroscopy, X-ray photo-electron spectroscopy (XPS) and transmission electron microscopy (TEM). The photocatalytic activity of the Pt/N-rGO/N-$NaNbO_3$ nanorod composites towards the hydrogen evolution has been investigated as well. It is interesting to find that an excellent hydrogen evolution rate of 2342 $\mu mol\, g^{-1}\, h^{-1}$ is attained by 0.5%Pt/0.5%N-rGO/N-$NaNbO_3$ under sunlight irradiation, much higher than those of both the pristine $NaNbO_3$ nanorod (241 $\mu mol\, g^{-1}\, h^{-1}$) presented in this work and several modified $NaNbO_3$ catalysts reported in the literatures elsewhere.

2. Experimental

GO is purchased from XFNASNO, and other reagents of analytical grade are purchased from Sinopharm Chemical Reagent Co., Ltd. All reagents are used without further purification.

2.1. Synthesis of NaNbO₃ composite

Precipitation method has been used for the synthesis of $NaNbO_3$ nanorods for which 1 g of niobium pentaoxide (Nb_2O_5) has been added to 11 M NaOH aqueous solution (60 mL) and kept it magnetic stirring with a moderate speed for 30 min. Then the intermixture has been transferred into a 100 mL Teflon-lined autoclave with a hydrothermal reaction (180 °C for 2 h). Subsequently, after filtering the solution, the filtrate has been washed by using deionized (DI) water and pure ethanol, and then dried at 100 °C overnight. Finally, the precipitates are calcined at 500 °C for 12 h.

2.2. Synthesis of N-rGO/N-NaNbO₃ composite

N-rGO/N-$NaNbO_3$ composites were firstly synthesized by a one-step hydrothermal calcinations method. Typically, GO (1 mg) has been dispersed in 50 mL DI water, then the above as-prepared $NaNbO_3$ (0.5 g) and urea (0.36 g) have been mixed with the suspension, followed by 1 h stirring. The mixture has been transferred into a 100 mL Teflon beaker with a hydrothermal reaction (180 °C for 12 h). Finally, the ground sample was washed thoroughly with DI water, dried at 100 °C and then calcined at 400 °C for 2 h under nitrogen atmosphere. A series of N-rGO/N-$NaNbO_3$ composites have been synthesized through varying the amounts of GO and urea while using the same method.

2.3. Synthesis of Pt/N-rGO/N-NaNbO₃ composite

The platinum nanoparticles-modified N-rGO/N-$NaNbO_3$ composites have been prepared by using the photo-deposition method. Typically, as-prepared N-rGO/N-$NaNbO_3$ composites (0.3 g) and 10 mg/mL aqueous $H_2PtCl_6 \cdot 6H_2O$ solution (0.42 mL) have been put into a beaker with 40 mL DI water and 9.5 mL methanol. And then the suspension has been irradiated by 300 W Xe light at 25 °C for 4 h under magnetic stirring. The sample was filtered, washed with DI water and then dried in a vacuum oven at 80 °C. Using the same method, the Pt NPs loaded $NaNbO_3$ catalyst has also been synthesized.

2.4. Materials characterization

The phase composition and crystalline nature were obtained on a D2 phaser X-ray diffractometer. TEM and HRTEM images were attained using a transmission electron microscopy (JOEL JEM 2010) operated at an accelerating voltage of 200 kV. XPS measurements were performed with a RBD 147 upgraded Perkin Elmer PHI 5000C ESCA system using Mg *Kα* radiation. And contaminant carbon (C 1s = 284.6 eV) was used to calibrate all binding energies. Elemental analysis (N, C and H) was determined by a VARIO EL III microanalyzer. FT-IR experiment was carried out with an AVATAR-360 Fourier Transform Infra-Red spectrometer. The band gaps of the samples were measured by Ultraviolet visible diffuse reflectance spectroscopy (UV–vis. DRS) carried out by a SHIMADZU UV-2450 spectrophotometer with $BaSO_4$ used as a reference. Photoluminescence (PL) spectra of powders were obtained with a JASCO FP-6500 fluorescence spectrophotometer at the emission wavelength of 300 nm.

2.5. Photocatalytic tests

The photocatalytic hydrogen evolution reaction was carried out in a gas recirculating closed system using a CEL-HXF300 300 W Xe arc lamp without a UV cutoff filter at room temperature. 20 mg of the photo-catalyst was suspended in 100 mL aqueous solution of methanol (CH_3OH) (20 vol.%). Then, the reactant solutions were degassed and irradiated. And the gases produced were analyzed through gas chromatograph fitted out with a 5 Å molecular sieve column and a thermal conductivity detector.

2.6. Photoelectrochemical tests

The electrochemical measurements were carried out by using an electrochemical station and an electrochemical analyzer (CHI660E) in a standard three-electrode quartz cell. The working electrode of photo-current was prepared as follows: the sample (3 mg) was ultrasonically dispersed in 1.0 mL of ethanol solution and then the mixture was applied to a clean FTO glass with a working area of 1 cm². After being dried at room temperature, the FTO glass was used as the working electrode, with a platinum plate as a counter electrode and a saturated calomel reference electrode. The transient photocurrent response of the different samples was determined in a 0.5 M Na_2SO_4 aqueous solution under irradiation of a 300 W Xe lamp without filter. The EIS plots were detected in mixed solution of potassium ferricyanide (0.025 M) and muriate of potash (0.1 M).

3. Results and discussion

3.1. Characterization of Pt/N-rGO/N-NaNbO₃

The morphology of the Pt/N-rGO/N-$NaNbO_3$ composites with different mass ratios is observed by TEM analyses, which discerns the presence of N-rGO and Pt NPs. The TEM image (Fig. 1a) shows that the synthesized pure $NaNbO_3$ are nanorods with a size of about 150 nm, and possess a smooth surface. In addition, for the 0.5%Pt/0.5%N-rGO/
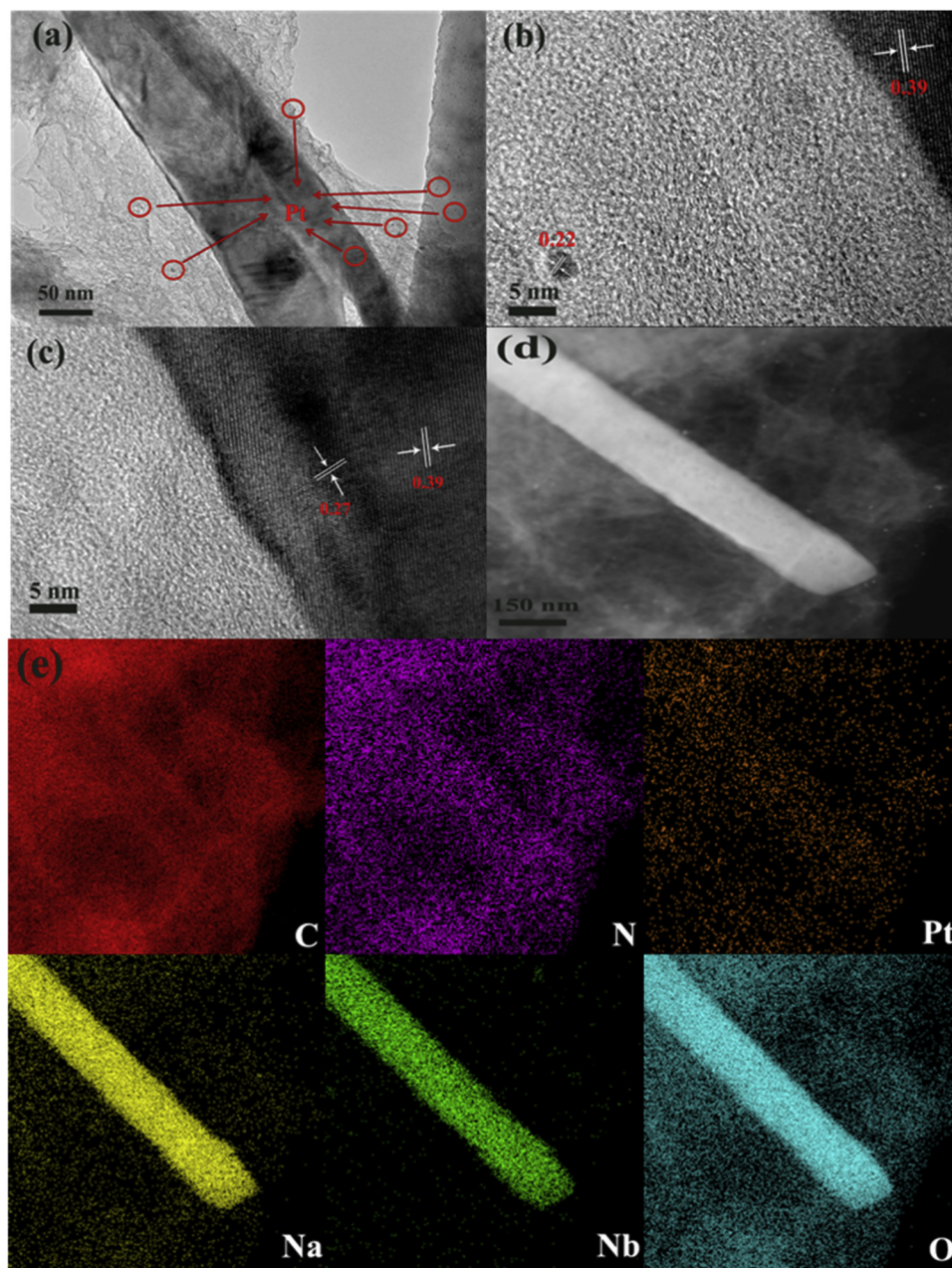
Fig. 1. (a) TEM, (b) and (c) HRTEM images of 0.5%Pt/0.5%N-rGO/N-NaNbO$_3$; (e) The corresponding EDX mapping images of C, N, Pt, Na, Nb and O in the area of (d).

N-NaNbO$_3$ (Fig. 1b and c), the layered structure of the stacked N-rGO sheets can be clearly seen. And the N-NaNbO$_3$ nanorods and Pt NPs (2.5 nm) are partly well distributed on the N-rGO nanosheets, as further evidenced by the clear lattice fringes of N-NaNbO$_3$ and Pt NPs with the interplanar spacing of 0.39, 0.27 and 0.22 nm, which corresponds to the (101), (200) facets of N-NaNbO$_3$ and (111) facet of Pt NPs, respectively. Furthermore, by utilizing energy dispersive X-ray (EDX) elemental mapping (Fig. 1e), Na, Nb, O, C, N, and Pt elements clearly emerge in the 0.5%Pt/0.5%N-rGO/N-NaNbO$_3$ composite, offering the convincing evidence of the successful combination Pt NPs, N-rGO and N-NaNbO$_3$. Especially, the N signal minor overlaps with the main Na, Nb and O signals, and most of them overlap with the main carbon signal, indicating that a small part of nitrogen element is successfully doped into NaNbO$_3$, while most of it is doped into the graphene. Based on the above results, it is suggested that Pt NPs, N-rGO and N-NaNbO$_3$ are well crystallized, and a close contact between Pt NPs, N-rGO and N-NaNbO$_3$

is noticed, which contribute to the fast separation of photogenerated electrons and holes.

To substantiate the above assumption, XRD characterization is carried out. Fig. 2 shows the XRD patterns of the Pt/N-rGO/N-NaNbO$_3$ composites with different mass ratios. As for pure NaNbO$_3$, the main peak at 2θ of 22.9°, 32.6°, 46.5°, 52.6°, 58.1° and 68.1° are assigned to the diffraction planes (001), (110), (002), (021), (112) and (022) of orthorhombic crystal phase of NaNbO$_3$ (JCPDS no. 33-1270). Compared to pure NaNbO$_3$, it seems that the doping of N element does not lead to notable structural changes for NaNbO$_3$ (Fig. S2). In addition, there is also no obvious signal of N-rGO phases detected in the XRD patterns of Pt/N-rGO/N-NaNbO$_3$ with different N-rGO content, as a result of the low content and comparatively low diffraction intensity of N-rGO. Moreover, because of the ultrafine nanoparticles and well dispersion of Pt on the surface of the N-NaNbO$_3$ and N-rGO, no signal about platinum can be detected in the XRD patterns of Pt/N-rGO/N-NaNbO$_3$.
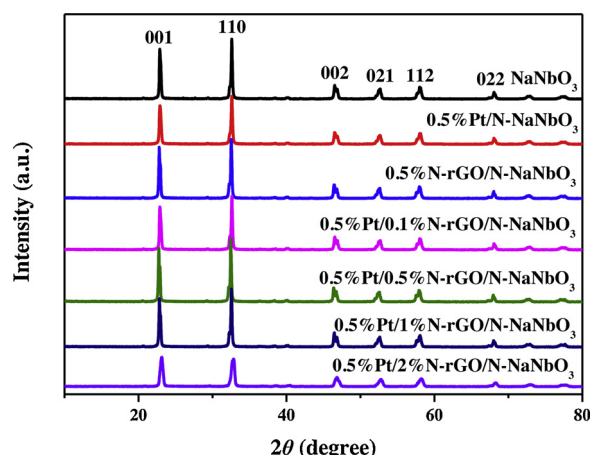
Fig. 2. XRD patterns of different photocatalysts.

Furthermore, there are no traces of any impurity phase under this resolution.

FT-IR and Raman spectra can further demonstrate the formation of Pt/N-rGO/N-NaNbO$_3$ photocatalysts. Raman scattering is an effectual approach to study the local distortions of crystal lattice. As shown in Fig. 3a, all Raman spectra have shown a strong characteristic peak near 600 cm^{-1} assigned to different Nb-O bond lengths [32,33], correlated with the stretching model of NbO$_6$ octahedron [34,35]. However, compared to the pristine NaNbO$_3$, the characteristic band of the Pt/N-rGO/N-NaNbO$_3$ composites are shifted towards lower wavenumber and remarkably broadened (Fig. 3b), while the characteristic band of NaNbO$_3$ treated with hydrothermal calcinations show no significant peak shifts (Fig. S3), revealing that the shift is caused by the interaction of N-rGO, Pt NPs and N-NaNbO$_3$ rather than the additional hydrothermal treatment and calcinations of NaNbO$_3$. The same conclusion can be drawn from the FT-IR spectra. As shown in Fig. 3c, the FT-IR spectra of the composites are in well lined with that reported in the literature. The broad peak near 600 cm^{-1} is assigned to the stretching model of Nb-O octahedron [36–38]. However, with the combination of N-rGO, Pt NPs and N-NaNbO$_3$, the peak shifts to a lower wavenumber, as depicted in Fig. 3d. These shifts in the Raman and FT-IR characteristic peak mirror the different NbO$_6$ octahedra local structure of the composites, which might affect the band structure of the NaNbO$_3$, leading to changes in the optical band gaps.

Moreover, the Raman spectra could also confirm the existence of nitrogen doped rGO in the Pt/N-rGO/N-NaNbO$_3$ composites. For comparison, the spectra of pristine GO and N-rGO under the same conditions are also collected (Fig. 3e). As is expected, GO displays two prominent G and D bands centered at around 1350 and 1600 cm^{-1}. The G band of the N-rGO is shifted to 1602 cm^{-1}, while the D band of the N-rGO is shifted to 1355 cm^{-1}. The D band is well-known linked to structural defects and disorder in graphene, and the G band is associated with the E2g vibration mode of sp2 carbon [39,40]. Moreover, with the increase of N-rGO content, the Raman spectra of 0.5%Pt/2%N-rGO/NaNbO$_3$ also exhibits the two typical D and G peaks (Fig. 3e). Compared with N-rGO, the D band of 0.5%Pt/2%N-rGO/N-NaNbO$_3$ shifts from 1330 to 1355 cm^{-1}, whereas the G band shifts from 1590 to 1602 cm^{-1}, indicating the presence of strong interaction between N-rGO sheet and Pt/N-NaNbO$_3$. Moreover, it is reported that the intensity ratio of D to G (I_D/I_G) provides the structural defect level in GO or graphene [41]. As expected, the I_D/I_G increased obviously from GO (0.90) to N-rGO (1.02), demonstrating a decrease of sp2 domain induced and a lower graphitic crystalline structure by the N-rGO [42]. Both the increasing of I_D/I_G and the shift of D and G bands demonstrate the existence of numerous defect sites and the successful introduction of nitrogen into GO in the Pt/N-rGO/N-NaNbO$_3$ composites, which may also contribute to the photocatalytic activity of the composites. This

result is further confirmed by the following XPS analysis.

The surface compositions and chemical states of the as-prepared ternary nanocomposites are investigated through XPS measurements of GO, N-rGO, NaNbO$_3$, N-NaNbO$_3$ and Pt/N-rGO/N-NaNbO$_3$ (Fig. 4a). It should be emphasized that the obvious N 1s signal in N-rGO and 0.5% Pt/0.5%N-rGO/N-NaNbO$_3$ confirms the successful doping of N element into GO and NaNbO$_3$. According to the XPS results, the N content of composites is listed in Table S1. The high resolution N 1s XPS spectra of the N-rGO shown in Fig. 4b is deconvoluted into four peaks centered at 399.3, 400.7, 401.6 and 402.5 eV, assigned to pyridinic N, pyrrolic N, graphitic N and oxidized pyridinic N, correspondingly [43], while the N 1s XPS spectra of N-NaNbO$_3$ in Fig. 4b is divided into two peaks at 399.0 and 395.4 eV, belonged to oxidized Nb-N (Nb-O-N) and Nb-N, correspondingly. The presence of N 1s peak of N-rGO and N-NaNbO$_3$ further confirms that nitrogen is successfully introduced into rGO and NaNbO$_3$. As shown in the N 1s XPS of the 0.5%Pt/0.5%N-rGO/N-NaNbO$_3$ composite, in addition to the above five typical types of nitrogen, the sixth N can be observed at a much low binding energy of 396.5 eV [44,45], probably attributing to the Pt-N formed by the interaction of Pt and N-rGO [46]. Moreover, it is found that the N 1s of 0.5%Pt/0.5%N-rGO/N-NaNbO$_3$ shifts to a lower binding energy, as a result of the interaction among the Pt, N-rGO and N-NaNbO$_3$ (Table S2). Due to the interaction in the composites, the electrons generated by the photo-excitation can be easily transmitted to the electron-rich center N atoms, resulting in a significant decrease in the N 1s binding energy.

The C 1s XPS peaks of the N-rGO (Fig. 4c) is centered at 284.6, 286.6 and 288.3 eV, corresponded to the C−C, C−N/C=O and C=N/C−O bond respectively [47,48]. The Pt 4f XPS peaks of the 0.5%Pt/N-NaNbO$_3$ and 0.5%Pt/0.5%N-rGO/N-NaNbO$_3$ catalysts are fitted with two transitions corresponding to the different oxidation states of Pt (Pt^0 and Pt^{2+}). The principle peaks of 0.5%Pt/0.5%N-rGO/N-NaNbO$_3$ are assigned to Pt^0 at 73.1 eV (4f$_{7/2}$) and 76.6 eV (4f$_{5/2}$), while the peaks at 74.9 and 78.3 eV are corresponded to Pt in the 2 + states [49]. The ratio results of different Pt species are calculated based on above data and listed in Table S3. The Pt^0 content of 0.5%Pt/0.5%N-rGO/N-NaNbO$_3$ sample is significantly higher than that of 0.5%Pt/N-NaNbO$_3$ sample, indicating that N species in N-rGO and N-NaNbO$_3$ act as electron-rich active sites to promote the reduction of Pt precursor. Moreover, a shift to higher energy is observed in the binding energies of the 0.5%Pt/0.5% N-rGO/N-NaNbO$_3$ catalyst, due to part of Pt donates electrons to N of N-rGO and N-NaNbO$_3$. This is consistent with the report that the polar functional groups induced by nitrogen doping can enhance the electronic affinity of the substrate and further promote the electronic donation behavior of platinum nanoparticles [50,51].

The Nb 3d XPS peaks of NaNbO$_3$ (Fig. 4e) centered at 206.7 eV (Nb 3d$_{5/2}$) and 209.4 eV (Nb 3d$_{3/2}$) are assigned to the Nb (+5) chemical state of NaNbO$_3$. Compared to the pure NaNbO$_3$, the Nb 3d peaks of N-NaNbO$_3$ migrate to lower binding energy, revealing the effect of N element doping into NaNbO$_3$. Furthermore, the Nb 3d XPS peaks of 0.5%N-rGO/N-NaNbO$_3$ and 0.5%Pt/0.5%N-rGO/N-NaNbO$_3$, centered at 206.7 and 209.4 eV, are fitted with the Nb (+5) chemical state of NaNbO$_3$, and two other new peaks with higher binding energy appear. The migration to the direction of higher binding energy indicates that N species in N-rGO and N-NaNbO$_3$ act as electron-rich active sites and the presence of Pt NPs and N-rGO both strongly interact with NaNbO$_3$, which drastically promotes the transfer of electrons. Due to the interaction in the composites, the electrons generated by the photo-excitation can be easily transmitted to the electron-rich center N atoms, resulting in a significant decrease in the N 1s binding energy and the increase in the Pt 4f and Nb 3d binding energy, revealing the interaction among the Pt, N-rGO and N-NaNbO$_3$. These XPS results reveal the successfully doped N element in rGO and NaNbO$_3$, and the effective interaction among Pt NPs, N-rGO and N-NaNbO$_3$.

Optical absorption properties have a crucial role in the photocatalytic activity of the catalysts. Fig. 5a shows the UV–vis DRS spectra
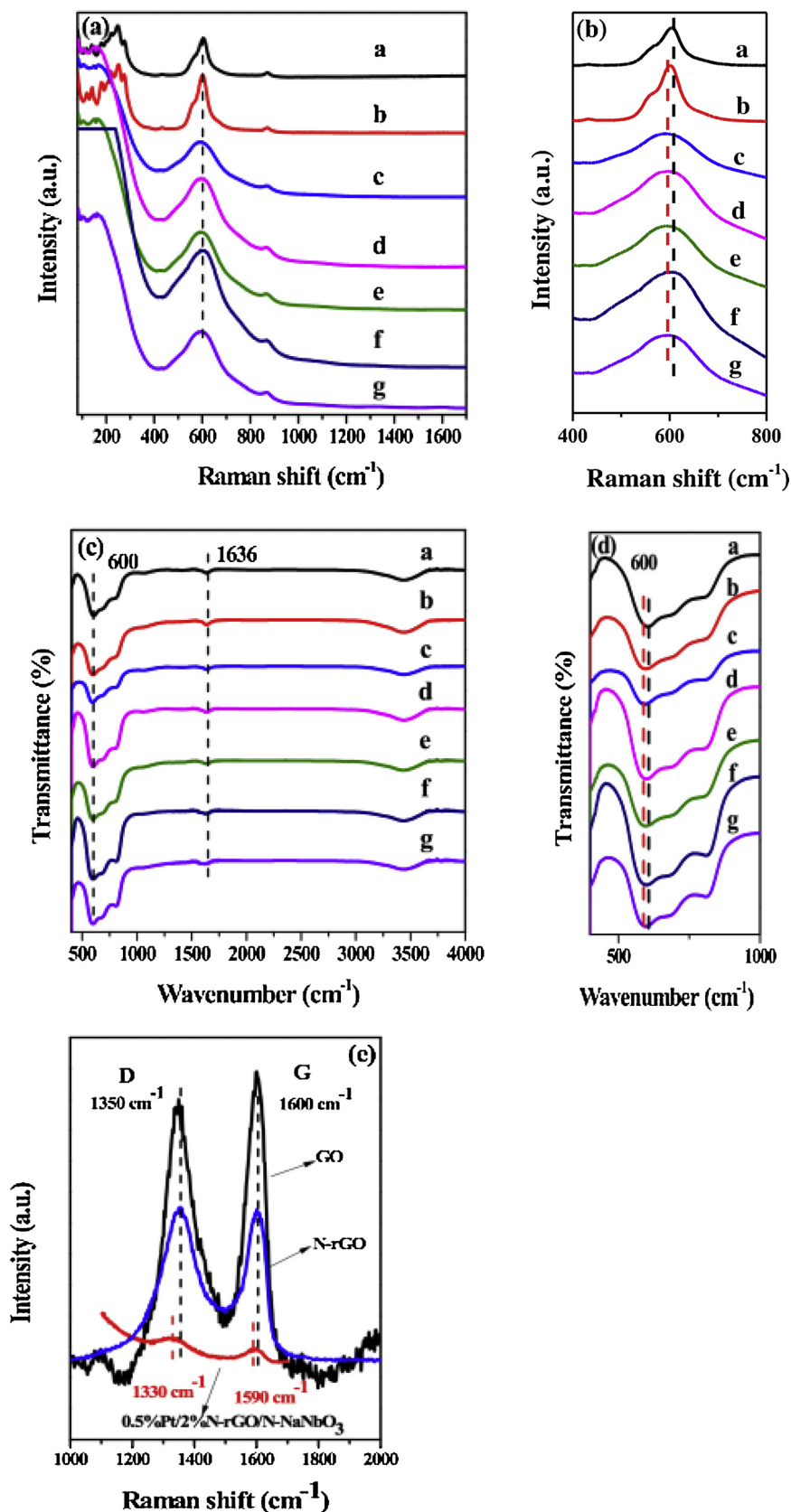
Fig. 3. Raman spectroscopy (a,b) and FT-IR spectra (c,d) of (a) NaNbO$_3$, (b) 0.5%Pt/N-NaNbO$_3$, (c) 0.5%N-rGO/N-NaNbO$_3$, (d) 0.5%Pt/0.1%N-rGO/N-NaNbO$_3$, (e) 0.5%Pt/0.5%N-rGO/N-NaNbO$_3$, (f) 0.5%Pt/1%N-rGO/N-NaNbO$_3$, (g) 0.5%Pt/2%N-rGO/N-NaNbO$_3$. (e) Raman spectra of GO, N-rGO and 0.5%Pt/2%N-rGO/N-NaNbO$_3$.
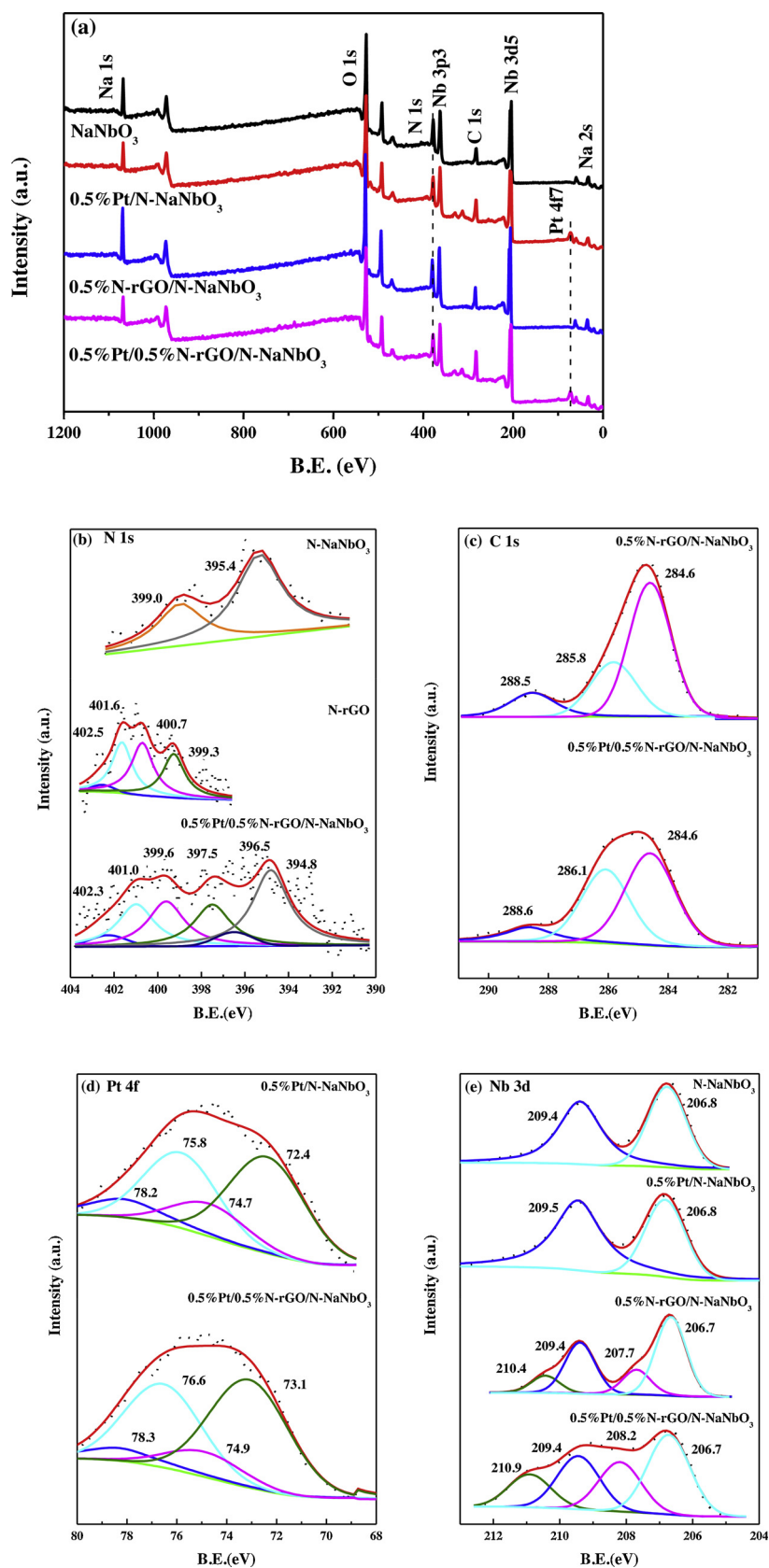
Fig. 4. XPS spectra of NaNbO₃, 0.5%Pt/N-NaNbO₃, 0.5%N-rGO/N-NaNbO₃ and 0.5%Pt/0.5%N-rGO/N-NaNbO₃: (a) Survey spectra, (b) N 1s, (c) C 1s, (d) Pt 4f, and (e) Nb 3d.
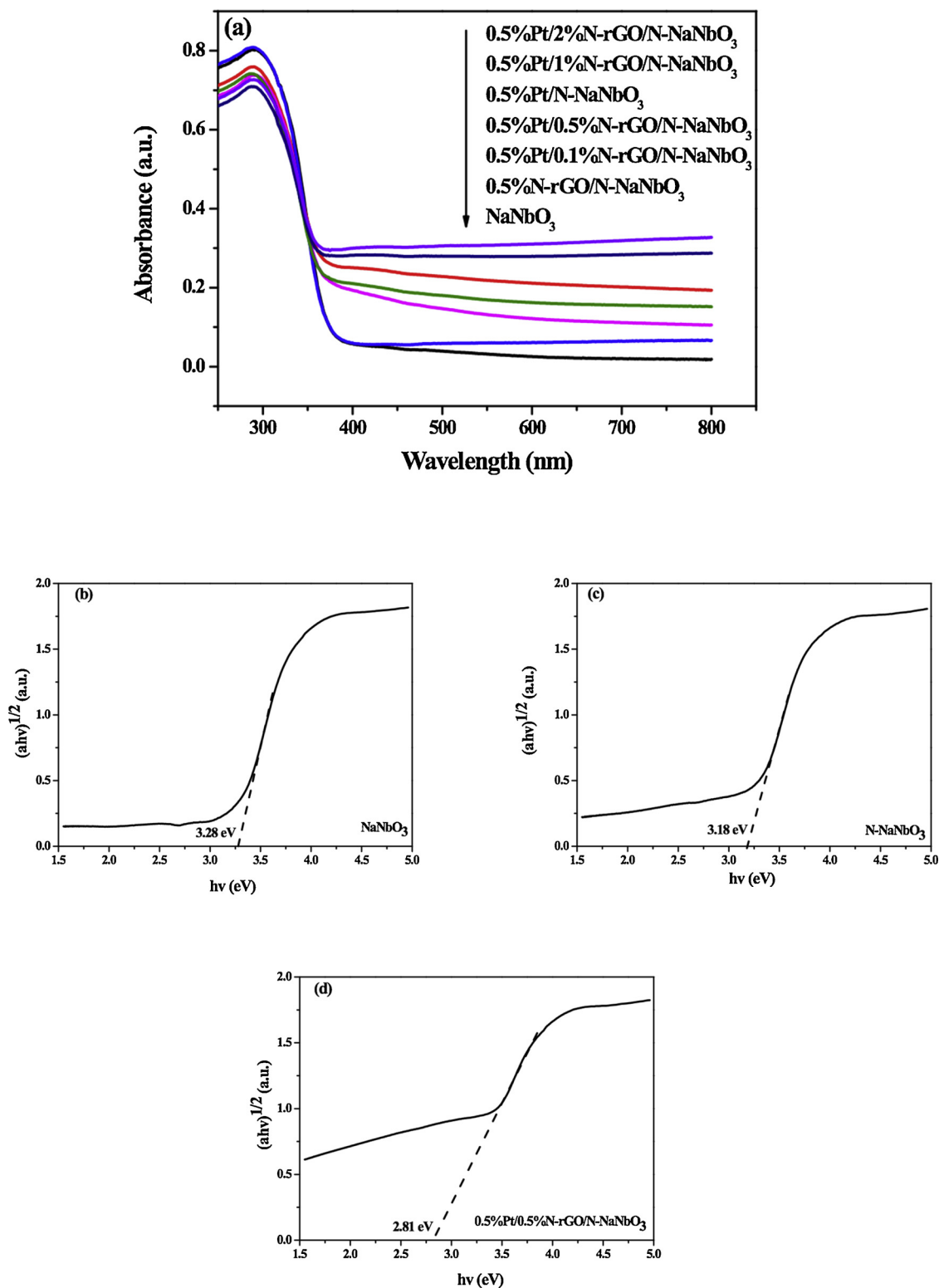
Fig. 5. (a) UV–vis. diffuse-reflectance spectra of different photocatalysts; the plot of $(\alpha h\nu)^{1/2}$ νs photon energy ($h\nu$) of the UV–vis. diffuse reflectance spectra of (b) NaNbO$_3$, (c) N-NaNbO$_3$, and (d) 0.5%Pt/0.5%N-rGO/N-NaNbO$_3$.

of a series of composites with an absorption edge at around 375 nm, caused by the transfer of electrons from the O 2p orbit (VB) to the Nb 4d orbit (CB) of NaNbO$_3$. The comparison of NaNbO$_3$ with N-NaNbO$_3$ (Fig. S4) shows that the doping of N element affects the absorption of light by NaNbO$_3$. In addition, according to the Tauc plots of $(\alpha h\nu)$ versus photon energy ($h\nu$) following the Kubelka-Munk method, the band gap of pure NaNbO$_3$ is around 3.28 eV, while that of N-NaNbO$_3$ decreases to

3.18 eV. Similarly, Pt/N-rGO/N-NaNbO$_3$ composites display a broad background absorption in the whole wavelength range studied, due to the presence of black N-rGO nanosheets. Moreover, the background increases with the increase of the N-rGO content, similar to the previously reported results [52]. Furthermore, the absorption edge redshifts slightly after loading with Pt NPs and N-rGO. These findings are ascribed to the existence of Pt NPs and N-rGO and the narrowing band
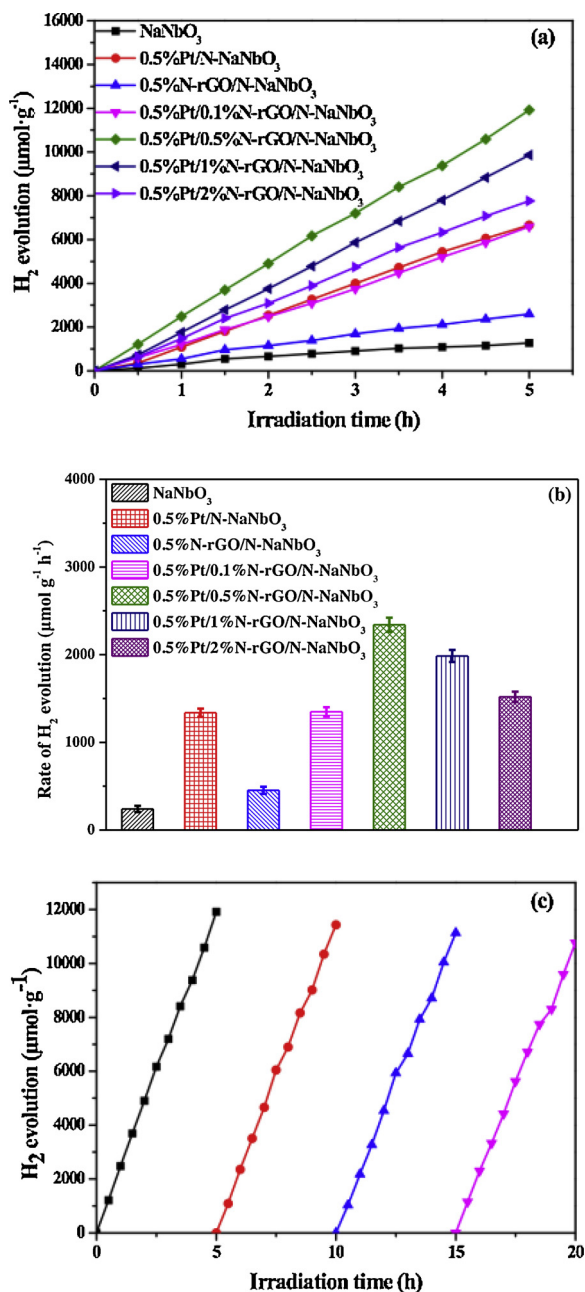
Fig. 6. Photocatalytic hydrogen evolution under sunlight irradiation (a), hydrogen evolution rates of various photocatalysts. The error bars are defined as s.d. (b) and reusability of 0.5%Pt/0.5%N-rGO/ N-NaNbO$_3$ for the photocatalytic hydrogen evolution (c).

gap of NaNbO$_3$ (Fig. S4). The calculated band gap of 0.5%Pt/0.5%N-rGO/N-NaNbO$_3$ is 2.81 eV. The electronic interaction and charge equilibration of Pt/N-rGO/N-NaNbO$_3$ result in a more pronounced shift in the Fermi level and a narrower band gap [53,54]. Owing to the extra p-electrons where N elements dedicate to the system, the N-rGO has better conductivity than the pristine rGO. Accordingly, N-rGO can act as a more ideal electron trap or electron transport medium. Such properties improve the effectiveness of the use of the light source. Photo-excited electrons and holes may therefore transfer quickly to the surface of N-rGO and Pt NPs to inhibit electron-hole pair recombination, which enhances the photocatalytic performance.

Table 1
The quantum efficiency (QE) for 0.5%Pt/0.5%N-rGO/N-NaNbO$_3$ tested through half reaction.

Wavelength/nm	320	350	420
QE/%	5.1	1.8	0.5

3.2. Photocatalytic activity test

Based on the above characterization results, the photocatalytic activities of the NaNbO$_3$ and the Pt/N-rGO/N-NaNbO$_3$ samples are evaluated with the photocatalytic hydrogen evolution in aqueous solution, using methanol as a scavenger under simulated illumination. It can be seen in Fig. 6a and b, the pristine NaNbO$_3$ displays very low photocatalytic H$_2$ production activity (241 μmol g^{-1} h^{-1}), and the N-rGO/N-NaNbO$_3$, Pt/N-NaNbO$_3$ and all the Pt/N-rGO/N-NaNbO$_3$ samples exhibit obviously higher photocatalytic activity. Moreover, the obvious increase of H$_2$ evolution rate over all the Pt/N-rGO/N-NaNbO$_3$ composites are observed. Among all the Pt/N-rGO/N-NaNbO$_3$ composites, 0.5%Pt/0.5%N-rGO/N-NaNbO$_3$ composite displays superior photocatalytic hydrogen generation activity (up to 2342 μmol g^{-1} h^{-1}), which is about 9, 6 and 2 times higher than that of pure NaNbO$_3$, N-rGO/N-NaNbO$_3$, and Pt/N-NaNbO$_3$. And the QE is calculated as about 5.1% (Table 1) at 320 nm. In addition, the photocatalytic performance of 0.5%Pt/0.5%N-rGO/N-NaNbO$_3$ is compared with the currently reported literature related to NaNbO$_3$ (Table S4). It is worth to note that the catalyst prepared herein has a higher hydrogen evolution activity than those reported in literature under the same reaction conditions. It can also be seen from the activity diagram that an appropriate amount of N-rGO is beneficial to the improvement of photocatalytic activity, but excessive N-rGO content will reduce the activity, owing to the redundant N-rGO blocking the absorption of visible light by NaNbO$_3$ and covering the active sites on the catalyst surface. Simultaneously, the long-term stability of photocatalysts is important for its next-step practical application. Due to the outstanding photocatalytic activity, the photostability of 0.5%Pt/0.5%N-rGO/N-NaNbO$_3$ catalyst is further studied. As shown in Fig. 6c, the rates of H$_2$ production are almost unanimous during four recycles, suggesting the good stability of photocorrosion resistance in photocatalytic hydrogen evolution. The highest hydrogen evolution rate is ascribed to the existence of Pt NPs and N-rGO: (1) with the introduction of N-rGO, light absorption over the entire wavelength range is enhanced; (2) the excellent electron transfer properties of N-rGO enable efficacious separation of electrons and holes; (3) Pt NPs act as electron traps to further effectively separate electron-hole pairs. In conclusion, graphene and Pt NPs play important roles in improving the photocatalytic performance of Pt/N-rGO/ N-NaNbO$_3$.

3.3. Reaction mechanism

In general, factors influencing photocatalytic performance of the catalysts mostly include the good light absorption, the separation rate of photoinduced electron-hole pairs and the specific surface area. However, the difference of the specific surface area of the composites (Fig. S5) is not significant, indicating that the modification does not significantly change the specific surface area, and thus affect the activity of the catalysts. And the 0.5%Pt/0.5%N-rGO/N-NaNbO$_3$ has a better light absorption than the pristine NaNbO$_3$, which has been confirmed by the results from UV–vis DRS. Moreover, it is well known that the separation rate of the photo-induced charged carriers of the photocatalysts normally links to the semiconductor photoexcitation and recombination/transport of the photoexcited charged carriers, which can be studied through probing the photochemical and photo-physical behaviors of electrons and holes. To further illuminate the above discussion results, photoluminescence (PL) spectroscopy, electrochemical
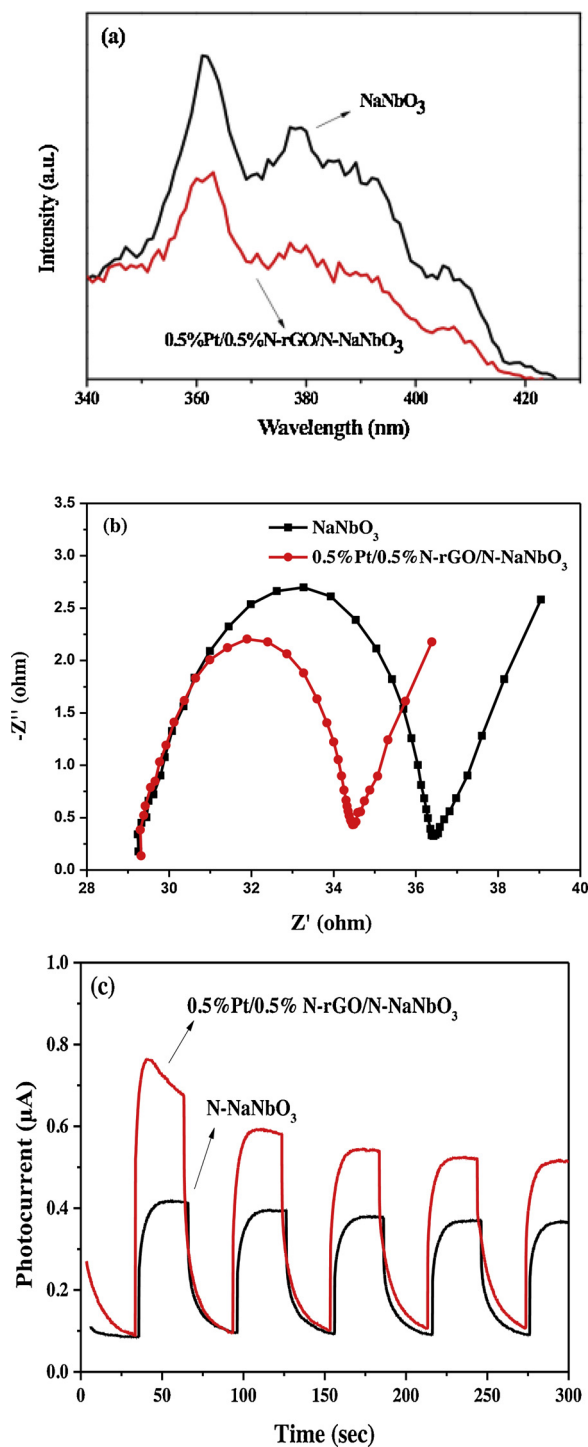
Fig. 7. Photoluminescene emission spectra (a), Electrochemical impedance spectra (b), and Photocurrent (c) of pristine NaNbO₃ and 0.5%Pt/0.5%N-rGO/N-NaNbO₃.

impedance spectroscopy (EIS) and photocurrent responses have been performed. Fig. 7a displays a comparison of the PL spectra of the pristine NaNbO₃ and 0.5%Pt/0.5%N-rGO/N-NaNbO₃. The results reveal that, under the excitation wavelength at 300 nm, both photocatalysts demonstrate alike emission profiles with the emission peak centered around 361 and 378 nm, originated from the localized states and defects of NaNbO₃ [55]. Compared with the pristine NaNbO₃, the 0.5%Pt/0.5%N-rGO/N-NaNbO₃ displayed an evidently decreased PL intensity, due to the high separation efficiency of electrons and holes.

To be more concise, EIS Nyquist plots of the composites are shown in Fig. 7b, which is an effective characterization to evaluate the charge transport, structure and conductivity of the materials. Generally, the charge-transfer resistance (Rct) is lower, and the diameter of the semicircle of the EIS spectra is smaller, illustrating the enhanced electron transfer capability and high separation effectiveness of photo-electron-hole. Manifestly, the 0.5%Pt/0.5%N-rGO /N-NaNbO₃ exhibits lower semicircle radius than the pristine NaNbO₃, further indicating that the introduction of Pt NPs and N-rGO obviously enhance the electron migration, and then reduce the recombination of charged carriers. In order to further verify the separation of the photogenerated electron-hole pairs, photoelectric current is obtained. As shown in Fig. 7c, the photoelectric current intensity of 0.5%Pt/0.5%N-rGO/N-NaNbO₃ is obviously higher than that of pristine NaNbO₃. The result is consistent with that of PL and EIS.

From the UV–vis. DRS results, the band gap of NaNbO₃, N-NaNbO₃ and 0.5%Pt/0.5%N-rGO/N-NaNbO₃ are estimated to be 3.28, 3.18 and 2.81 eV, respectively. Fig. S6 reveals the valence band XPS (VB XPS) spectra of NaNbO₃, N-NaNbO₃ and 0.5%Pt/0.5%N-rGO/N-NaNbO₃. The location of the valence band edges of NaNbO₃, N-NaNbO₃ and 0.5% Pt/0.5%N-rGO/N-NaNbO₃ are at *ca.* 2.17, 1.98 and 1.61 eV$_{NHE}$, respectively. As reported in the literatures, band structure of NaNbO₃ is primarily composed of Nb 3d and O 2p, and the substitutional N-doping leads to band gap narrowing because of efficacious hybrid of 2p orbitals of N and O orbitals [56]. Furthermore, the introduction of N-rGO and Pt NPs further affects its band structure. Based on the above discussions, Fig. 8 exhibits the complete band structure of NaNbO₃, N-NaNbO₃ and 0.5%Pt/0.5%N-rGO/N-NaNbO₃.

As shown in Fig. 9, a possible photocatalytic reaction mechanism is illustrated. Under the simulated sunlight illumination, the VB electrons of N-NaNbO₃ are excited to the CB, creating holes in the VB. The holes oxidize methanol to other oxidation products such as formaldehyde, while electrons can reduce H⁺ in water through three ways to generate hydrogen. Some of the electrons react directly to produce hydrogen and the other parts are transferred to Pt NPs for further reaction, and the remainings are transferred to the N-rGO and then transferred to Pt NPs for further reaction. According to the literature results previously reported, the photoexcited electrons move from N-rGO to Pt NPs is energetically favorable [57,58]. In the above process, the separation efficiency of electron-hole pairs can be greatly improved due to the excellent transfer properties of N-rGO and Pt NPs. It is worthy of noticing that in comparison with the pristine NaNbO₃, the photocatalytic performance of 0.5%Pt/0.5%N-rGO/NaNbO₃ is significantly improved. Doping of N element into NaNbO₃ narrows its bang gap. In addition, N-rGO in the nanocomposite not only improves the absorption of the light, but also effectively separates photogenerated electron-hole pairs as Pt NPs does. For N-rGO, the doping of nitrogen element can make the
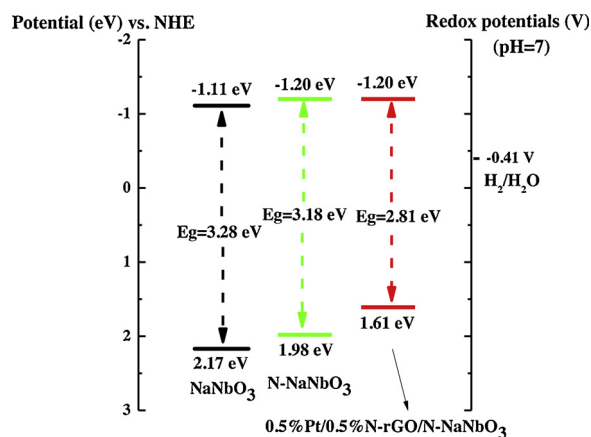

Fig. 8. Schematic illustration of band structures of NaNbO₃, N-NaNbO₃ and 0.5%Pt/0.5%N-rGO/N-NaNbO₃.
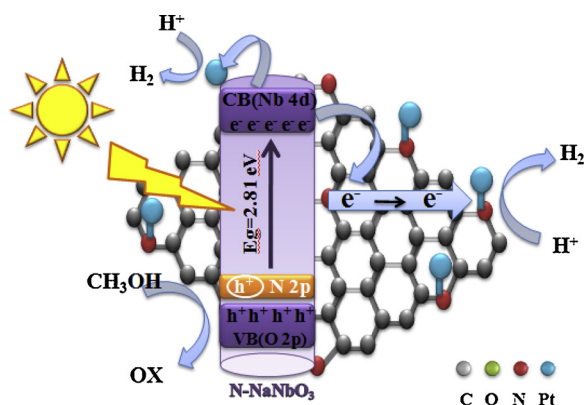
Fig. 9. Schematic illustration of the mechanism of 0.5%Pt/0.5%N-rGO/ N-NaNbO₃ during photocatalytic hydrogen evolution under sunlight irradiation.

defect sites accompanied by the effective reduction of GO the smallest, leading to a great electrical conductivity. All these reasons result in the enhancing photocatalytic activity of 0.5%Pt/0.5%N-rGO/N-NaNbO₃.

4. Conclusion

A novel facile method of successfully synthesizing the N-doped NaNbO₃ nanorods decorated by N-doped graphene nanosheets (Pt/N-rGO/N-NaNbO₃) is reported in this work where Pt NPs are evenly distributed. In the photocatalytic hydrogen evolution, 0.5%Pt/0.5%N-rGO/N-NaNbO₃ nanorod not only exhibits 9-fold higher activity than that of pristine NaNbO₃, but also displays high stability, which was not reported till now for modified sodium niobate. The quantum efficiency (QE) value of 0.5%Pt/0.5%N-rGO/N-NaNbO₃ reaches 5.1% at the wavelength of 320 nm. The notably enhanced photocatalytic activity is ascribed to the unique structure of Pt/N-rGO/N-NaNbO₃ composites. The doping of nitrogen element makes the band gap of NaNbO₃ narrow, and the defect sites accompanied by the effective reduction of GO the smallest as well, leading to a great electrical conductivity. Moreover, the introduction of N-rGO enhances the light absorption over the entire range of wavelength. The improvement of electron-hole separation rate is effectively increased due to the excellent electron transfer properties of N-rGO and Pt NPs. The present work might provide a useful strategy for further development of efficient hydrogen photocatalysts, a comprehensive knowledge for which is considered likely to facilitate sustainable production to meet the increasing energy demand worldwide.

Conflict of interest

There is no interest to declare.

Acknowledgements

Appendix A. Supplementary data

Supplementary data associated with this article can be found, in the online version, at https://doi.org/10.1016/j.apcatb.2019.117901.

References

[1] B. Naik, S.M. Kim, C.H. Jung, S.Y. Moon, S.H. Kim, J.Y. Park, Enhanced H₂ generation of Au-loaded, nitrogen-doped TiO₂ hierarchical nanostructures under visible light, Adv. Mater. Interfaces 1 (2014) 201300018, , https://doi.org/10.1002/admi.201300018.

[2] F.L. Yang, J. Ren, Q.Q. Liu, L. Zhang, Y.Y. Chai, W.L. Dai, Facile oxalic acid-assisted construction of laminated porous N-deficient graphitic carbon nitride: highly efficient visible-light-driven hydrogen evolution photocatalyst, J. Energy Chem. 33 (2019) 1–8, https://doi.org/10.1016/j.jechem.2018.08.002.

[3] X.B. Li, J. Xiong, J.T. Huang, Z.J. Feng, J.M. Luo, Novel g-C₃N₄/h'ZnTiO₃-a'TiO₂ direct Z-scheme heterojunction with significantly enhanced visible-light photocatalytic activity, J. Alloys. Compd. 774 (2019) 768–778, https://doi.org/10.1016/j.jallcom.2018.10.034.

[4] D.P. Kumar, S. Hong, D.A. Reddy, T.K. Kim, Noble metal-free ultrathin MoS₂ nanosheet-decorated CdS nanorods as an efficient photocatalyst for spectacular hydrogen evolution under solar light irradiation, J. Mater. Chem. A Mater. Energy Sustain. 4 (2016) 18551–18558, https://doi.org/10.1039/C6TA08628D.

[5] K. Iwashina, A. Kudo, Rh-doped SrTiO₃ photocatalyst electrode showing cathodic photocurrent for water splitting under visible-light irradiation, J. Am. Chem. Soc. 133 (2011) 13272–13275, https://doi.org/10.1021/ja2050315.

[6] Y.C. Chen, Y.K. Hsu, R. Popescu, D. Gerthsen, Y.G. Lin, C.J.N.C. Feldmann, Au@Nb@HₓK₁₋ₓNbO₃ nanopeapods with near-infrared active plasmonic hot-electron injection for water splitting, Nat. Commun. 9 (2018) 232–243, https://doi.org/10.1038/s41467-017-02676-w.

[7] M. Machida, J.I. Yabunaka, T. Kijima, Synthesis and photocatalytic property of layered perovskite tantalates, RbLnTa₂O₇ (Ln = La, Pr, Nd, and Sm), Chem. Mater. 12 (2000) 812–817, https://doi.org/10.1021/cm990577j.

[8] H. Kato, H. Kobayashi, A. Kudo, Role of Ag⁺ in the band structures and photocatalytic properties of AgMO₃ (M: Ta and Nb) with the perovskite structure, J. Phys. Chem. B 106 (2002) 12441–12447, https://doi.org/10.1021/jp025974n.

[9] J. Wan, Y. Pu, C. Hui, C. Cui, Y. Guo, Effect of KNbO₃ on microstructure and electrical properties of lead-free 0.92BaTiO₃–0.08K₀.₅Bi₀.₅TiO₃ ceramic, J. Mater. Sci. Mater. Electron. 29 (2018) 1–8, https://doi.org/10.1007/s10854-018-8639-6.

[10] X. Dong, Y. Song, J. Yu, C. Min, F. Wei, S. Wei, Ag-decorated AtaO₃ (A = K, Na) nanocube plasmonic photocatalysts with enhanced photocatalytic water-splitting properties, Langmuir 31 (2015) 9694–9699, https://doi.org/10.1021/acs.langmuir.5b01294.

[11] H. Shi, G. Chen, C. Zhang, Z. Zou, Polymeric g-C₃N₄ coupled with NaNbO₃ nanowires toward enhanced photocatalytic reduction of CO₂ into renewable fuel, ACS Catal. 4 (2014) 3637–3643, https://doi.org/10.1021/ca500848f.

[12] L. Peng, X. Hua, L. Liu, T. Kako, N. Umezawa, H. Abe, Constructing cubic-orthorhombic surface-phase junctions of NaNbO₃ towards significant enhancement of CO₂ photoreduction, J. Mater. Chem. A 2 (2014) 5606–5609, https://doi.org/10.1039/c4ta00105b.

[13] F. Fresno, P. Jana, P. Renones, J.M. Coronado, D.P. Serrano, CO₂ reduction over NaNbO₃ and NaTaO₃ perovskite photocatalysts, Photochem. Photobiol. Sci. 16 (2017) 17–23, https://doi.org/10.1039/C6PP00235H.

[14] S. Chen, Y. Hu, J. Lei, X. Jiang, X. Fu, Preparation and characterization of direct Z-scheme photocatalyst Bi₂O₃/NaNbO₃ and its reaction mechanism, Appl. Surf. Sci. 292 (2014) 357–366, https://doi.org/10.1016/j.apsusc.2013.11.144.

[15] D. Kumar, S. Singh, N. Khare, Plasmonic Ag nanoparticles decorated NaNbO₃, nanorods for efficient photoelectrochemical water splitting, Int. J. Hydrogen Energy 43 (2018) 8198–8205, https://doi.org/10.1016/j.ijhydene.2018.03.075.

[16] Y. Wei, G. Tan, H. Ren, X. Ao, Y. Luo, L. Yin, Enhanced photocatalytic of N/F-doped-NaTaO₃ photocatalyst synthesized by hydrothermal method, J. Mater. Sci. Mater. Electron. 25 (2014) 3807–3815, https://doi.org/10.1007/s10854-014-2093-x.

[17] S. Kumar, R. Parthasarathy, A.P. Singh, B. Wickman, M. Thirumal, A. Gang, Dominant {100} facet selectivity for enhanced photocatalytic activity of NaNbO₃ in NaNbO₃/CdS core/shell heterostructures, Catal. Sci. Technol. 7 (2017) 481–495, https://doi.org/10.1039/C6CY02098D.

[18] S. Meng, Q. Yan, S. Yu, C. Wang, Y. Tao, P. Ji, B. Du, Facile fabrication of BiOI decorated NaNbO₃ cubes: a p–n junction photocatalyst with improved visible-light activity, Appl. Surf. Sci. 416 (2017) 288–295, https://doi.org/10.1016/j.apsusc.2017.04.136.

[19] B.C. Luo, H.J. Dong, D.Y. Wang, K. Jin, Large recoverable energy density with excellent thermal stability in Mn-modified NaNbO₃-CaZrO₃ lead-free films, J. Am. Ceram. Soc. 101 (2018) 3460–3467, https://doi.org/10.1111/jace.15528.

[20] S. Weon, J. Kim, W. Choi, Dual-components modified TiO₂ with Pt and fluoride as deactivation-resistant photocatalyst for the degradation of volatile organic compound, Appl. Catal. B. Environ. 220 (2018) 1–8, https://doi.org/10.1016/j.apcatb.2017.08.036.

[21] S.M. Lam, J.A. Quek, J. Sin, Mechanistic investigation of visible light responsive Ag/ZnO micro/nanoflowers for enhanced photocatalytic performance and antibacterial activity, J. Photochem. Photobiol. A 353 (2018) 171–184, https://doi.org/10.1016/j.jphotochem.2017.11.021.

[22] J. Wu, B. Liu, Z. Ren, M. Ni, C. Li, Y. Gong, W. Qin, Y. Huang, C.Q. Sun, X. Liu, CuS/RGO hybrid photocatalyst for full solar spectrum photoreduction from UV/Vis to near-infrared light, J. Colloid Interface Sci. 517 (2018) 80–85, https://doi.org/10.1016/j.jcis.2017.09.042.

[23] S. Prabhu, S. Manikumar, L. Cindrella, O. Kwon, Charge transfer and intrinsic electronic properties of rGO-WO₃ nanostructures for efficient photoelectrochemical and photocatalytic applications, Mater. Sci. Semicond. Proc. 74 (2018) 136–146, https://doi.org/10.1016/j.mssp.2017.10.041.

[24] R. Yousefi, J. Beheshtian, S.M. Seyed-Talebi, H.R. Azimi, F. Jamali-Sheini, Experimental and theoretical study of enhanced photocatalytic activity of Mg-doped ZnO NPs and ZnO/rGO nanocomposites, Chem. Asian J. 13 (2018) 194–203, https://doi.org/10.1002/asia.201701423.

[25] B. Koo, S. Byun, S. Nam, S. Moon, S. Kim, J.Y. Park, B.T. Ahn, B. Shin, Reduced graphene oxide as a catalyst binder: Greatly enhanced photoelectrochemical stability of Cu(In,Ga)Se₂, photocathode for solar water splitting, Adv. Funct. Mater. 28

(2018) 1705136, , https://doi.org/10.1002/adfm.201705136.

[26] H. Li, S. Wang, M. Feng, J. Yang, B. Zhang, Self-assembly and performances of wrinkled rGO@carbon fiber with embedded SnO₂ nanoparticles as anode materials for structural lithium-ion battery, J. Mater. Sci. 53 (2018) 11607–11619, https://doi.org/10.1007/s10853-018-2401-6.

[27] M. Pedrosa, L.M. Pastrana-Martínez, M.F.R. Pereira, J.L. Faria, J.L. Figueiredo, N/S-doped graphene derivatives and TiO₂ for catalytic ozonation and photocatalysis of water pollutants, Chem. Eng. J. 348 (2018) 888–897, https://doi.org/10.1016/j.cej.2018.04.214.

[28] M.H. Elbakkay, W.M.A.E. Rouby, S.I. El-Dek, A. Farghali, S-TiO₂/S-reduced graphene oxide for enhanced photoelectrochemical water splitting, Appl. Surf. Sci. 439 (2018) 1088–1102, https://doi.org/10.1016/j.apsusc.2018.01.070.

[29] J.F. Chang, L. Shuang, W. Qian, High reversible capacity of nitrogen-doped graphene as an anode material for lithium-ion batteries, Adv. Mater. Res. 1070-1072 (2015) 459–464, https://doi.org/10.4028/www.scientific.net/amr.1070-1072.459.

[30] L. Zhang, Y. Shi, W. Liang, C. Hu, AgBr-wrapped Ag chelated on nitrogen-doped reduced graphene oxide for water purification under visible light, Appl. Catal. B. Environ. 220 (2017), https://doi.org/10.1016/j.apcatb.2017.08.038.

[31] X.P. Bai, X. Zhao, W. Fan, Preparation and enhanced photocatalytic hydrogen-evolution activity of ZnGa₂O₄/N-rGO heterostructures, RSC Adv. 7 (2017) 53145–53156, https://doi.org/10.1039/C7RA09981A.

[32] S. Park, H.J. Song, C.W. Lee, S.W. Hwang, I. Cho, Enhanced photocatalytic activity of ultrathin Ba₅Nb₄O₁₅ two-dimensional nanosheets, ACS Appl. Mater. Interfaces 7 (2015) 21860–21867, https://doi.org/10.1021/acsami.5b06281.

[33] A. Kania, K. Roleder, G.E. Kugel, M. Fontana, Raman scattering, central peak and phase transitions in AgNbO₃, J. Phys. Chem. 19 (1986) 9–20, https://doi.org/10.1088/0022-3719/19/1/007.

[34] H.W. Eng, P.W. Barnes, B.M. Auer, P.M. Woodward, Investigations of the electronic structure of d0 transition metal oxides belonging to the perovskite family, J. Solid State Chem. 175 (2003) 94–109, https://doi.org/10.1016/s0022-4596(03)00289-5.

[35] G. Li, T. Kako, D. Wang, Z. Zou, J. Ye, Composition dependence of the photophysical and photocatalytic properties of (AgNbO₃)₁₋ₓ(NaNbO₃)ₓ solid solutions, J. Solid State Chem. 180 (2007) 2845–2850, https://doi.org/10.1016/j.jssc.2007.08.006.

[36] V. Shanker, S.L. Samal, G.K. Pradhan, C. Narayana, A. Ganguli, Nanocrystalline NaNbO₃ and NaTaO₃: rietveld studies, Raman spectroscopy and dielectric properties, Solid State Sci. 11 (2009) 562–569, https://doi.org/10.1016/j.solidstatesciences.2008.08.001.

[37] G. Blasse, G. Heuvel, Vibrational and electronic spectra and crystal structure of cubic Na₃NbO₄, Mater. Res. Bull. 7 (1972) 1041–1043, https://doi.org/10.1016/0025-5408(27)90156-0.

[38] Y. Shiratori, A. Magrez, K. Kasezawa, M. Kato, S. Rohrig, F. Peter, C. Pithan, R. Waser, Noncentrosymmetric phase of submicron NaNbO₃ crystallites, J. Electroceram. 19 (2007) 273–280, https://doi.org/10.1007/s10832-007-9032-7.

[39] L.S. Panchakarla, A. Govindaraj, C. Rao, Nitrogen- and boron-doped double-walled carbon nanotubes, ACS Nano 1 (2007) 494–500, https://doi.org/10.1021/nn700230n.

[40] K.N. Kudin, B. Ozbas, H.C. Schniepp, R.K. Prud'Homme, I.A. Aksay, R. Car, Raman spectra of graphite oxide and functionalized graphene sheets, Nano Lett. 8 (2008) 36–41, https://doi.org/10.1021/nl071822y.

[41] N. Tian, Z. Li, D. Xu, Y. Li, W. Peng, G. Zhang, F. Zhang, X. Fan, Utilization of MoS₂ nanosheets to enhancethe photocatalytic activity of ZnO for the aerobic oxidation of benzyl halides under visible light, Ind. Eng. Chem. Res. 55 (2016) 8726–8732, https://doi.org/10.1021/acs.iecr.6b01420.

[42] D. Geng, C. Ying, Y. Chen, Y. Li, R. Li, X. Sun, S. Ye, S. Knights, High oxygen-reduction activity and durability of nitrogen-doped graphene, Energy Environ. Sci.

4 (2011) 760–764, https://doi.org/10.1039/C0EE00326C.

[43] A. Pendashteh, J. Palma, M. Anderson, R. Marcilla, NiCoMnO₄ nanoparticles on N-doped graphene: highly efficient bifunctional electrocatalyst for oxygen reduction/evolution reactions, Appl. Catal. B. Environ. 201 (2017) 241–252, https://doi.org/10.1016/j.apcatb.2016.08.044.

[44] D. He, Y. Jiang, H. Lv, M. Pan, S. Mu, Nitrogen-doped reduced graphene oxide supports for noble metal catalysts with greatly enhanced activity and stability, Appl. Catal. B. Environ. 132 (2013) 379–388, https://doi.org/10.1016/j.apcatb.2012.12.005.

[45] P. Kuo, W. Chen, H. Huang, I. Chang, S.A. Dai, Stabilizing effect of pseudo-dendritic polyethylenimine on platinum nanoparticles supported on carbon, J. Phys. Chem. B 110 (2006) 3071–3077, https://doi.org/10.1021/jp055688m.

[46] A. Alain, M.M. Chehimi, G. Iluminada, P. Jean, V. Neus, Electrochemical oxidation of aliphatic amines and their attachment to carbon and metal surfaces, Langmuir 20 (2004) 8243–8253, https://doi.org/10.1021/la049194c.

[47] W. Tu, Z. Yong, L. Qi, S. Yan, S. Bao, X. Wang, X. Min, Z. Zou, An in situ simultaneous reduction-hydrolysis technique for fabrication of TiO₂-graphene 2D sandwich-like hybrid nanosheets: graphene-promoted selectivity of photocatalytic-driven hydrogenation and coupling of CO₂ into methane and ethane, Adv. Funct. Mater. 23 (2013) 1743–1749, https://doi.org/10.1002/adfm.201202349.

[48] T. Peng, L. Kan, Z. Peng, Q. Zhang, X. Zhang, Enhanced photocatalytic hydrogen production over graphene oxide–cadmium sulfide nanocomposite under visible light irradiation, J. Phys. Chem. C 116 (2012) 22720–22726, https://doi.org/10.1021/jp306947d.

[49] P. Bera, K.R. Priolkar, A. Gayen, P.R. Sarode, M.S. Hegde, S. Emura, R. Kumashiro, V. Jayaram, G. Subbanna, Ionic dispersion of Pt over CeO₂ by the combustion method: structural investigation by XRD, TEM, XPS, and EXAFS, Chem. Mater. 34 (2003) 2049–2060, https://doi.org/10.1021/cm0204775.

[50] T. Varga, G. Varga, H. Haspel, A. Kukovecz, Z. Konya, One step synthesis of chlorine-free Pt/nitrogen-doped graphene composite for oxygen reduction reaction, Carbon 133 (2018) 90–100, https://doi.org/10.1016/j.carbon.2018.03.020.

[51] Y. Zhou, T. Holme, J. Berry, T. Ohno, D. Ginley, R. O'Hayre, Dopant-induced electronic structure modification of HOPG surfaces: implications for high activity fuel cell catalysts, J. Phys. Chem. C 114 (2010) 506–515, https://doi.org/10.1021/jp9088386.

[52] Q. Xiang, J. Yu, M. Jaroniec, Synergetic Effect of MoS₂ and graphene as cocatalysts for enhanced photocatalytic H₂ production activity of TiO₂ nanoparticles, J. Am. Chem. Soc. 134 (2012) 6575–6578, https://doi.org/10.1021/ja302846n.

[53] Z. Lan, G. Zhang, X. Wang, A facile synthesis of Br-modified g-C₃N₄ semiconductors for photoredox water splitting, Appl. Catal. B. Environ. 192 (2016) 116–125, https://doi.org/10.1016/j.apcatb.2016.03.062.

[54] Q. Xiang, J. Yu, M. Jaroniec, Graphene-based semiconductor photocatalysts, Chem. Soc. Rev. 41 (2012) 782–796, https://doi.org/10.1039/c1cs15172j.

[55] S. Chen, L. Ji, W. Tang, X. Fu, Abrication, characterization and mechanism of a novel Z-scheme photocatalyst NaNbO₃/WO₃ with enhanced photocatalytic activity, Dalton Trans. 42 (2013) 10759–10768, https://doi.org/10.1039/C3DT50699A.

[56] N.K. Veldurthi, R.R. Jitta, G. Ravi, R. Guje, R. Velchuri, P. Venkataswamy, M. Vithal, Fabrication and visible–light induced photocatalytic activity of NaNbO₃ oriented composite photocatalyst coupled with N-NaNbO₃ and V-NaNbO₃, Chemistryselect 1 (2016) 2783–2791, https://doi.org/10.1002/slct.201600484.

[57] B.M. Bang, H. Kim, H.K. Song, J. Cho, S. Park, Scalable approach to multi-dimensional bulk Si anodes via metal-assisted chemical etching, Energy Environ. Sci. 4 (2011) 5013–5019, https://doi.org/10.1039/clee02310a.

[58] C.X. Guo, H.B. Yang, Z.M. Sheng, Z.S. Lu, Q. Song, C. Li, Layered graphene/quantum dots for photovoltaic devices, Angew. Chem. Int. Ed. 49 (2010) 3014–3017, https://doi.org/10.1002/anie.200906291.